Spatial-feedback control of dispersive chaos in binary-fluid convection

Paul Kolodner[1] and Georg Flätgen[1,2,3]
[1]*Bell Laboratories, Lucent Technologies, Inc., Murray Hill, New Jersey 07974*
[2]*Fritz-Haber-Institut der Max-Planck-Gesellschaft, Berlin, Germany*
[3]*Department of Chemical Engineering, Princeton University, Princeton, New Jersey 07974*
(Received 10 September 1999)

Dispersive chaos is a dynamical state that consists of the repeated, irregular growth and abrupt decay of spatially localized bursts of traveling waves. This state can be observed just above onset in convection in binary fluids at small, negative separation ratio ψ, in a long, quasi-one-dimensional geometry. We describe experiments in which this erratic behavior is suppressed by applying as feedback a spatially varying Rayleigh-number profile computed from the measured convection pattern. With the appropriate feedback algorithm, an initial state consisting of unidirectional traveling waves of spatially uniform amplitude and wave number can be maintained in a steady state over a large fraction of the unstable branch of the subcritical bifurcation to convection. This allows us to measure the nonlinear coefficients of the corresponding quintic complex Ginzburg-Landau equation.

PACS number(s): 05.45.Gg, 47.20.Ky, 47.54.+r, 47.62.+q

INTRODUCTION

In the last decade, there has been intense interest among physicists in feedback stabilization of systems which exhibit chaos in the absence of control. While the theory of control has been a branch of mathematics and engineering for decades, it was the pioneering paper of Ott, Grebogi, and Yorke [1] which was responsible for triggering this latest wave of activity in the dynamical-systems community. Soon after this theoretical work was published, experimentalists began demonstrating the feasibility of using feedback for the stabilization of real chaotic systems [2].

It has long been appreciated that feedback control of erratic spatiotemporal patterns in spatially extended systems is a much more general and difficult problem than control of single-channel or ''lumped'' dynamical systems. There have been many different theoretical and computational approaches to this problem. Several groups have studied spatiotemporal chaos in coupled-map lattices (CML's), exploring the effect of applying feedback at discrete subsets of the lattice sites [3]. In general, the spatial density of control sites necessary for stabilization increases as the number of positive Lyapunov exponents increases. However, in convectively unstable systems, in which the effects of feedback at one spatial point propagate downstream, a lower density of control sites may be required for stabilization [4]. In some systems, modeled by PDE's instead of CML's, the dynamics are such that control at a single spatial point can cause a regular dynamical state to invade the entire system [5]. There have also been several papers in which it has been assumed that feedback can be applied continuously in space and/or time. Strategies based on continuous time-delayed and/or space-shifted feedback have proven effective in stabilizing periodic patterns in systems which would exhibit erratic spatiotemporal behavior in the absence of feedback [6].

Experimental work on feedback control of spatially extended systems is much less advanced. Bocaletti *et al.* used time-delayed feedback to stabilize a periodic state in an effectively one-dimensional experiment on Bénard-Marangoni convection [7]. By using a Karhunen-Loève decomposition to reduce spatiotemporal dynamics to a single-channel time series, Qin, Wolf, and Chang were able to apply standard feedback techniques to stabilize the temperature fluctuations exhibited during the oxidation of CO on a two-dimensional catalytic wafer [8]. In both of these experiments, feedback was applied globally; i.e., to a single parameter which sets the spatiotemporal dynamics of the entire system. Stabilization of unstable dynamics using true, spatially varying feedback has been the subject of only two previous experiments, both concerned with Rayleigh-Bénard convection [9,10]. In a quasi-one-dimensional geometry, Howle [9] was able to stabilize the quiescent state at Rayleigh numbers above the onset of convection by applying feedback to a line of heaters on the underside of the bottom plate of the cell. Feedback was computed from shadowgraph images of the flow pattern. Tang and Bau [10] similarly suppressed the onset of convection in a two-dimensional convection cell, using feedback based on signals from an array of temperature sensors in the interior of the fluid layer. These two experiments were designed to suppress steady convection above onset, not to stabilize an erratic spatiotemporal pattern.

Binary-fluid convection in a long, narrow, annular cell is an excellent physical system for exploring the control of spatiotemporal dynamics with spatially distributed feedback. The first instability observed in this system, as the Rayleigh number is increased above onset, is to small-amplitude traveling waves (TW's) [11]. Because the signals produced by this instability and the nonlinear states it triggers are oscillatory, low-frequency drifts can be eliminated using demodulation techniques, allowing high-precision, stable data acquisition [12]. Above onset, the TW's grow in amplitude, making a transition to a nonlinear state whose qualitative features depend on the separation ratio ψ. This concentration-dependent parameter describes the extent to which buoyancy is modified by the Soret effect [13]. For negative ψ, nonlinear TW's with spatially uniform and time-independent wave-number and amplitude profiles can be created. Frequency-corrected shadowgraph images of these

TW's, processed using the technique of complex demodulation [12], can be used to construct accurate wave-number and amplitude reference images. These references allow high-precision measurements of the structure of other dynamical states in the same apparatus [14]. For $\psi \lesssim -0.07$, it is also possible to create a nonlinear state consisting of localized regions of TW's which drift through the system at constant velocity without change of shape [15]. The drift velocity of these TW ''pulses'' depends sensitively on the local Rayleigh number, and this sensitivity can be exploited to precisely measure and compensate small spatial variations in the Rayleigh number, using local heaters attached to the underside of the convection cell. As described below, this compensation can be automated and used to apply nonuniform Rayleigh-number profiles, computed as feedback from real-time measurements of the TW amplitude and wave-number profiles. Finally, the dynamics observed in this system are slow enough to be followed in detail in real time. Thus this experiment presents an ideal system for sensitively testing the effect of spatial feedback on spatiotemporal dynamics.

Depending on parameters, nonlinear TW convection can exhibit secondary instabilities and spatiotemporal chaos, and these dynamics are amenable to control by spatial feedback. For $\psi \gtrsim -0.04$, bringing the Rayleigh number above onset leads, after a long transient, to a persistent state in which spatially localized regions of TW's form, grow in amplitude, shrink in space, and abruptly collapse. This process repeats erratically, producing a spatiotemporally chaotic state whose fluctuations are statistically stationary. Because these irregular dynamics have been shown to have their origin in strong nonlinear dispersion, this state has been called ''dispersive chaos'' [16,17]. We have used spatial feedback to suppress this erratic behavior. Using a series of feedback algorithms, we have stabilized a state of unidirectional TW's with spatially uniform amplitude and wave number far onto an unstable TW branch which is born from the quiescent state via a subcritical bifurcation. By tracing this unstable branch, we have accurately measured the nonlinear coefficients of the complex Ginzburg-Landau equation (CGLE) which describes this bifurcation. In a previous publication [18], we briefly described our experimental techniques and the results obtained. In this paper, we discuss in greater detail the physical system, the feedback algorithms used for stabilization, and their implications for future work.

The rest of this paper is organized as follows. In the next section, we review the CGLE model which has been used to describe the nonlinear evolution of TW's in this system. Next, we describe the apparatus and the procedures used to acquire and analyze data and to apply nonuniform spatial feedback in response to the observed TW pattern. The following section discusses calibration experiments which have to be carried out to enable feedback control of TW's and describes how uniform TW's are created as an initial condition for feedback control and how the data are corrected for drifts and optical distortions. The specific feedback algorithms used for this control, and the results obtained with this feedback, are described in the next section. Finally, in the Discussion section, we describe limitations of the present experiments and future applications of the feedback techniques we have developed.

THE COMPLEX GINZBURG-LANDAU-EQUATION MODEL

In our discussion of spatial feedback algorithms and data analysis below, it will be useful to have at hand a few results obtained from the CGLE model of TW convection. Because the applicability of this model to this system has been considered extensively in the general literature and in Ref. [17] in particular, we shall merely write down the appropriate version of the CGLE with minimal justification. Since this system exhibits a subcritical bifurcation to TW's, we retain nonlinear terms to fifth order. Because the experiments concern TW states which are extremely uniform in space, we do not include any nonlinear gradient terms. Finally, since we study only unidirectional TW's, we do not retain any terms representing a coupling with the oppositely propagating TW component. Thus the quintic CGLE for the complex TW amplitude $\tilde{A}(x,t)$ reads

$$\tau_0(\partial_t + s\partial_x)\tilde{A} = \varepsilon(1+ic_0)\tilde{A} + \xi_0^2(1+ic_1)\partial_x^2\tilde{A} + g(1+ic_2)|\tilde{A}|^2\tilde{A} + h(1+ic_4)|\tilde{A}|^4\tilde{A}. \tag{1}$$

Here, τ_0 is a characteristic time, s is the linear TW group velocity, ξ_0 is a correlation length, $g>0$ and $h<0$ are nonlinear saturation parameters, and c_i, $i=0,1,2,4$ are dispersion coefficients. The linear coefficients τ_0, s, ξ_0^2, and $c_{0,1}$ and the nonlinear dispersion coefficient c_2 have been experimentally measured under conditions close to those of the present experiments [17,19]. In flow-visualization experiments, the pattern amplitude $|\tilde{A}|$ is proportional to the gain of the visualization system, which is difficult to estimate with precision. Therefore measurements of the absolute magnitudes of the saturation parameters g and h are uncertain to within a scale factor.

There are two regimes in which we will find it useful to obtain results from Eq. (1). The first of these is one in which global and spatial feedback are applied in order to control a state of unidirectional TW. By ''global and spatial feedback,'' we mean that we apply a stress parameter ε which is the sum of a component which varies only in time (the global component) and one or more components which vary in space as well as time (the spatial components). Thus

$$\varepsilon(x,t) = \varepsilon_g(t) + \Delta\varepsilon_1(x,t) + \Delta\varepsilon_2(x,t) + \ldots . \tag{2}$$

The global feedback component $\varepsilon_g(t)$ is computed from measurements of the spatially averaged pattern amplitude $A_s = \langle|\tilde{A}(x,t)|\rangle$, using an algorithm described below. The spatial-feedback components $\Delta\varepsilon_1(x,t)$, $\Delta\varepsilon_2(x,t)$, etc., are computed using algorithms that were separately developed to tame instabilities that arose sequentially in the experiments. The main result of this paper is that, with suitable algorithms for computing the global and spatial feedback components, it is possible to maintain the system in a state of unidirectional TW's whose complex amplitude is time-independent and spatially uniform over a wide range of amplitudes A_s, even though the uncontrolled system evolves erratically. This uniform controlled state is maintained by feedback of infinitesimal magnitude—that is, the deviations of $\varepsilon(x,t)$ from its

average value (to which we refer for the moment simply as ε) are close to the experimental noise level. In this regime, we may insert $\tilde{A}(x,t)=A_s e^{i(\Delta\omega t-\Delta k x)}$ into Eq. (1) to obtain

$$\varepsilon-\xi_0^2\Delta k^2+gA_s^2+hA_s^4=0, \tag{3a}$$

$$\tau_0\Delta\omega=s\Delta k+c_0\varepsilon-c_1\xi_0^2\Delta k^2+c_2gA_s^2+c_4hA_s^4. \tag{3b}$$

Equations (3a) and (3b) represent the bifurcation diagram and nonlinear dispersion relation of the controlled TW state, respectively. The quantitative results of our experiments will be fit to these equations.

Let us now consider a second regime, in which Eq. (1) describes the initial destabilization of a small-amplitude TW state in the absence of feedback control. Following Kaplan, Kuznetsov, and Steinberg [19,20], we retain only the important terms in the cubic part of the CGLE, rescaling so that $\tau_0=\xi_0=g=1$ and $c_{0,1}=0$ and setting $h=0$. With $\tilde{A}(x)=A(x,t)\exp[i\phi(x,t)]$ and $\Delta k(x,t)=-\partial_x\phi(x,t)$, we obtain

$$(\partial_t+s\partial_x)\Delta k=\partial_x[A^{-2}\partial_x(A^2\Delta k)]-c_2\partial_x A^2, \tag{4a}$$

$$(\partial_t+s\partial_x)A=(\varepsilon-\Delta k^2)A+\partial_x^2A+A^3. \tag{4b}$$

At very small TW amplitude, the source term $c_2\partial_x A^2$ in Eq. (4a) is negligible. In this regime, nonuniformities in Δk vanish, and the natural TW state is one of uniform wave number. However, because $|c_2|\gg 1$, if the amplitude grows sufficiently large, then this term becomes important in regions of local amplitude nonuniformities, leading to the growth of corresponding local deviations in the wave number. These in turn reinforce the amplitude nonuniformities, via a local reduction in the linear growth rate $\varepsilon-\Delta k^2$ in Eq. (4b). Thus above a threshold amplitude, the system loses stability to the growth of localized amplitude gradients. In Ref. [17], we verified that this mechanism does indeed describe the initial destabilization of uniform TW's and leads to the development of dispersive chaos. Equations (4a) and (4b) suggest a feedback stabilization algorithm that will be described in the Discussion section below.

APPARATUS AND PROCEDURES

In this section, we briefly review aspects of our experimental apparatus that have been the subject of previous publications [14,15], and we describe new features related to the application of spatial feedback in detail. The convection cell is a long, narrow annulus, formed by a disc and ring machined from ULTEM 1000 polyetherimide plastic which are clamped between a mirror-polished, silicon bottom plate and a transparent, sapphire top plate. The annular channel has height $d=0.2597(2)$ cm, radial width $\Gamma_r=2.074(3)d$, and mean circumference $\Gamma_\phi=91.10(8)d$ (we also ran experiments in cells of slightly different geometries to obtain some of the qualitative results mentioned in this paper). Wave numbers and frequencies are rendered nondimensional by scaling with the cell height d and the vertical thermal diffusion time $\tau_v=d^2/\kappa=45.8$ sec, respectively, where κ is the thermal diffusivity of the fluid filling the cell. As usual, the Rayleigh number R is proportional to ΔT, the temperature difference applied between the bottom and top plates of the cell, and we define the stress parameter $\varepsilon\equiv(R-R_{\rm ref})/R_{\rm ref}$. Here, $R_{\rm ref}$ is a reference Rayleigh number, usually defined by the onset of convection. In these experiments, ε is assumed to have a spatial variation.

The top plate of the convection cell is cooled by circulating water which is swirled over the sapphire window to enhance azimuthal uniformity. The water temperature is measured by a thermistor in contact with the top plate and is regulated to ± 0.5 mK by a dc bridge and a temperature regulator. ΔT is read by an ac thermistor bridge which serves as the input to a second temperature-regulation system. This system drives two electrical heaters on the underside of the bottom plate of the cell which are wired in parallel. A round, 50-Ω, thin-film heater glued to the center of the plate produces about 80% of the heat required for the temperature control. The remaining heat is provided by a second system, which is used to control the spatial profile of the bottom-plate temperature. This system consists of 24 $\frac{1}{10}$-W, 100-Ω resistors, uniformly spaced and pressed against the underside of the bottom plate in a ring just outside the footprint of the convection cell. Each trim heater is wired in series with a variable shunt resistor which is used to adjust its power dissipation. In previous experiments, ordinary variable resistors were used for these adjustments [15]. In the present experiments, these have been replaced by Xicor X9312 series nonvolatile digital potentiometers [21], controlled by transistor-transistor logic (TTL) pulses generated by a computer running Labview software. The voltage on each of the trim heaters is restricted to the range 0.06–4.5 V and is controlled with a precision of about 1 mV, as compared with the total heater voltage of 13.5–15.1 V. As described below, this system allows us to impose an arbitrary Rayleigh-number profile, including one that is nominally uniform, with a fractional azimuthal variation of $1-2\times10^{-4}$rms, as measured using the pulse-drift technique [15]. Because of hardware and software improvements, this uniformity is about two times better than we have reported previously [14,15]. Given a desired Rayleigh-number profile, an optimization program calculates the required 24 heater voltages, and a Labview program applies them to the trim heaters. This process takes 60–90 sec on a 75-MHz Pentium computer. The fractional temporal stability of the spatially averaged temperature difference applied across the convection cell is $2-5\times10^{-5}$ rms over time scales shorter than a day. Drifts over longer periods are removed as described below and previously [14,17].

Two ethanol/water mixtures were used in these experiments. For the calibration experiments described in the next section, we used a 2.8 wt % ethanol solution at a mean temperature of 27.95 °C, with separation ratio $\psi=-0.124$, Prandtl number Pr=6.78, and Lewis number $L=0.0084$ [13], to match the parameters in Refs. [14] and [15]. Experiments on control of dispersive chaos were performed using a 0.4 wt % solution at a mean temperature of 27.60 °C. For this fluid, $\psi=-0.020$, Pr=5.92, and $L=0.0085$ [13].

In this system, convection patterns can in general take the form of superpositions of clockwise- and counterclockwise-propagating TW's of the form $A(x)\sin[k(x)x\pm\omega(x)t]$. In the experiments described here, we have dealt exclusively with unidirectional TW patterns whose amplitude, wave number, and oscillation frequency $A(x)$, $k(x)$, and $\omega(x)$ vary only on spatial scales much longer than $2\pi/k_m$ (in this paper, the subscript m denotes the spatial average of a measured pro-

file). The mean wave number of these TW patterns is quantized by the finite geometry of our convection cell, and, because of the narrow gain curve of the linear instability in this system [17], the small-amplitude state observed at onset, after the decay of transients, has a mean wave number $k_m = 2\pi N_r/\Gamma_\phi = 3.035$, where $N_r = 44$ is the number of wavelengths filling the convection cell. We have restricted our experiments at higher amplitudes to observations of this quantized state. Near onset, the typical oscillation period $\tau_{\rm osc} = 2\pi/\omega_m$ is 90–100 sec.

The TW pattern is monitored using a shadowgraph system [12,14] and is recorded at 360 azimuthal locations by a circular array of photodiodes whose signals are sampled by two computers. One computer, used only for independent quantitative data acquisition when the dynamics have been verified to be stable, samples the system at a rate $\sim 4/\tau_{\rm osc}$ for many oscillation cycles. Complex demodulation of this signal [12] is used to extract $A(x)$ and $k(x)$ with a precision of $\pm 3\%$ in A and $\pm 0.2\%$ in k. Demodulation of the time series at several spatial points yields the oscillation frequency ω_m with a fractional precision of $\sim 1\times 10^{-4}$. These calculations are the source of the data displayed in Fig. 15 below.

The complex demodulation program described in Ref. [12] does not require that the data be sampled at a particular rate with respect to the oscillation period, as long as the true oscillation frequency can be determined *post hoc*, and aliasing is avoided. However, because of the narrow temporal bandwidth required for accurate results, this procedure is not fast enough for real-time feedback control. Thus a second computer, dedicated to fast control of the system, samples the photodiode data exactly four times per cycle, and we have developed a fast demodulation routine that exploits this synchronization to produce amplitude and wave-number profiles from only four such samples, using previous measurements of the oscillation period to determine the correct sampling rate. These profiles are used to compute the feedback Rayleigh-number profile applied to the convection cell, which is updated once per time step $\Delta t = 200-220$ sec during control experiments. We have found that the wave-number profiles produced by this fast demodulation routine exactly match those produced by full complex demodulation, but the amplitude profiles are distorted by noise at low amplitudes. The consequences of this distortion will be discussed below.

CALIBRATIONS, INITIAL CONDITIONS, AND DATA REDUCTION

We begin this section by briefly reviewing the techniques developed in Refs. [14,15] for measuring and correcting the spatial profiles of the amplitude, wave number, and Rayleigh number, using time-independent TW states at $\psi = -0.124$. These experiments were performed at constant applied temperature difference and with a nominally uniform spatial Rayleigh-number profile. The first calibration was made by creating a state of fully nonlinear TW's of nominally uniform amplitude and wave number, with $N_r = 44$. As in Ref. [14], the wave-number and amplitude profiles in this state were measured at several different Rayleigh numbers and linearly extrapolated to zero TW velocity to obtain reference profiles which are unaffected by thermal nonuniformities in the apparatus. Typical profiles measured in this manner are shown in Fig. 1. Both profiles exhibit a weak second-harmonic component which is caused by small distortions in the optical system [12,14]. The amplitude profile exhibits an rms spatial variation of about 5%; this is stable to about $\pm 3\%$ in time. The wave-number profile exhibits a 0.5% rms spatial variation and a temporal stability of 0.2% rms. As described below and in Ref. [14], these profiles can be used as references to correct distortions in measurements of the structures of other dynamical states with a precision of about 3% in amplitude and 0.2% in wave number.

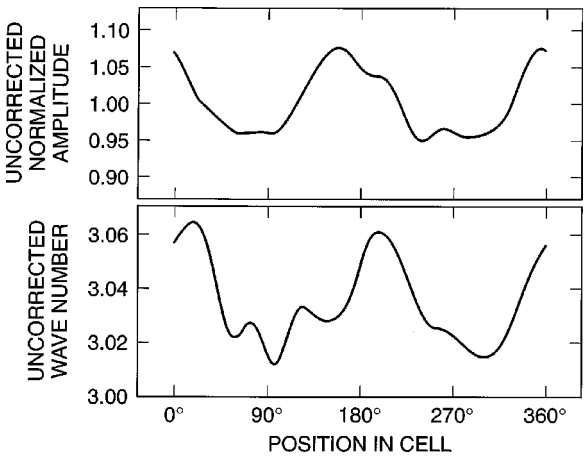

FIG. 1. Uncorrected amplitude (top) and wave-number (bottom) profiles for a state of uniform TW at $\psi = -0.124$, after linear extrapolation to zero TW velocity. The spatial dependence of these reference profiles is dominated by weak distortions in the optical system. The TW's in this and all states discussed in this paper propagate to the right.

After this calibration of the optical system, drifting pulses were used to measure and correct the spatial uniformity of the local Rayleigh number. As in Ref. [15], a uniform Rayleigh-number profile is obtained by iteratively measuring the spatial variation of the pulse drift velocity $v_{\rm dr}$ and adjusting the voltages on the trim heaters until $v_{\rm dr}$ is uniform, since $v_{\rm dr}$ depends strongly and monotonically on the local Rayleigh number. The spatial variation of the Rayleigh number can be reduced to $\lesssim 1\times 10^{-4}$ in this manner, although this uniformity degrades somewhat in time. The measurement of reference profiles and the adjustment of the Rayleigh-number uniformity were iterated several times to obtain the best possible compensation of thermal nonuniformities and optical distortions.

To verify that we understand the gain of our trim-heater system and the dependence of the pulse drift velocity on the local Rayleigh number, we computed the trim-heater voltages necessary to produce known, nonuniform Rayleigh-number profiles, installed the calculated voltages, and measured the resulting drift-velocity profiles. Figure 2 shows a typical result. The smooth curve shows the desired, sine-shaped Rayleigh-number profile. The irregular curve shows the measured drift-velocity profile, converted to Rayleigh number. The agreement between the two curves demonstrates that a nonuniform Rayleigh-number profile can be applied with a precision of $1-2\times 10^{-4}$.

We now turn to the initiation and calibration of controlled TW states at small amplitude at $\psi = -0.020$. In these experi-

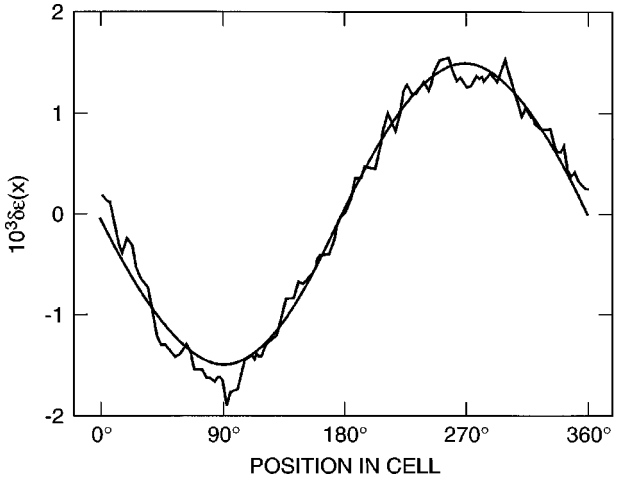

FIG. 2. The fractional deviation of the Rayleigh number is plotted as a function of position for an experiment in which a sine-shaped Rayleigh-number profile (smooth curve) is imposed on the convection cell. The rough curve shows measurements of the actual Rayleigh number, made using the pulse-drift technique at $\psi = -0.124$. The two curves agree to within $1-2\times10^{-4}$ rms.

ments, we operate the apparatus in an unusual mode: the independent parameter that is used as a set point is not the Rayleigh number but the spatially averaged TW amplitude A_s. Feedback causes the Rayleigh number to vary in time as required to keep A_s stable and in space as necessary to keep the amplitude and wave-number profiles uniform. We begin each experimental run by creating a uniform reference state at $A_s = A_{\rm ref} = 0.0024$. This amplitude is smaller than the thresholds of any spatial instabilities and can be maintained by global feedback alone, with a spatially uniform Rayleigh number. We initiate these experiments by injecting localized disturbances into the cell, allowing these to decompose into oppositely propagating packets of small-amplitude TW's, and suppressing TW's that propagate in the undesired direction [15]. Linear dispersion turns the remaining TW's into a spatially uniform, unidirectional state in about 10 h (this process can be accelerated using the spatial feedback described below). During this evolution, A_s is kept equal to $A_{\rm ref}$ by global feedback, using the control algorithm described in Ref. [12]. This algorithm is equivalent to the proportional and derivative components of standard proportional-integral-derivative control. To implement this control, we make periodic measurements of the amplitude growth rate $\gamma = A_m^{-1} dA_m/dt$ and of the fractional amplitude error $\Delta = \ln(A_m/A_s)$. At intervals of 900 to 1300 sec, we subtract a correction $\eta_1\gamma + \eta_2\Delta$ from the latest applied stress parameter $\varepsilon_g(t)$, where $\eta_{1,2}$ are positive feedback gain constants. Equation (1) implies that the derivative gain η_1 should be set equal to the characteristic time τ_0 for efficient control. In practice, we use a somewhat smaller gain to avoid oscillations. The proportional gain η_2 is set empirically. This global feedback is applied during all measurements described in this paper (at higher amplitudes, where additional spatial feedback components are required for stability, we find that the system develops inertia and requires a weak integral component for stability). After transients have decayed, we measure the Rayleigh number $R_{\rm ref}$, the spatially averaged TW frequency $\omega_{\rm ref}$, and the wave-number and amplitude profiles $A_{\rm ref}(x)$ and $k_{\rm ref}(x)$, all averaged over several hours for noise reduction.

This reference-state measurement was repeated approximately weekly during the course of our control experiments. In between these calibrations, we acquired shadowgraph data at other values of the set point A_s, holding A_s constant after a jump and imposing global and spatial feedback as required to produce stable, uniform amplitude and wave-number profiles. Changes in A_s caused the TW frequency derived from the shadowgraph data and the Rayleigh number to settle to new average values which we denote $\omega(A_s)$ and $R(A_s)$, respectively. As in Refs. [14] and [17], we used the reference measurements of $\omega_{\rm ref}$ and $R_{\rm ref}$ to correct these measurements for small drifts, which we attribute to slow preferential absorption of water by the plastic walls of the convection cell. The references $\omega_{\rm ref}$ and $R_{\rm ref}$ were interpolated smoothly in time, and intervening measurements made at different values of A_s were drift corrected by computing $\Delta\omega(A_s) = \omega_m(A_s) - \omega_{\rm ref}$ and $\varepsilon(A_s) = [R(A_s) - R_{\rm ref}]/R_{\rm ref}$. This drift correction introduces uncertainties of $1-2\times10^{-4}$ in both $\Delta\omega/\omega_{\rm ref}$ and ε.

The reference profiles $A_{\rm ref}(x)$ and $k_{\rm ref}(x)$ are used to correct the optical distortions discussed above in connection with Fig. 1. As in Ref. [14], measurements of $A(x)$ and $k(x)$ made at other values of A_s are corrected by computing $A(x)/A_{\rm ref}(x)$ and $k(x) - k_{\rm ref}(x) + k_m$. When we speak of the uniformity of the amplitude and wave-number profiles in this paper, we will be referring to these corrected profiles. As mentioned previously, we have found that the wave-number profile measured in the small-amplitude reference state at $A_s = A_{\rm ref}$ is stable and matches that measured at $\psi = -0.124$ (bottom of Fig. 1) to within the quoted uncertainty of about 0.2% rms. In contrast, the amplitude profile measured at $A_s = A_{\rm ref}$ is rather variable in time and differs significantly from that shown in Fig. 1. Given this discrepancy, it is important to ask whether $A_{\rm ref}(x)$ and $k_{\rm ref}(x)$ are indeed reliable reference profiles which are insensitive to such experimental artifacts such as nonuniformities and noise. One clue is clarifying this issue comes from the experiment whose result is shown in Fig. 3. Here, after establishing a stable TW state at $A_s = A_{\rm ref}$, we produced a localized nonuniformity in $\varepsilon(x)$ by turning up the voltage on one of the trim heaters. This caused the amplitude profile to become strongly nonuniform [the spatial derivative of $A(x)$ resembles the Rayleigh-number profile, with a slight broadening of the peak but no spatial shift], while the wave-number profile is completely unaffected. These observations are consistent with Eqs. (4a) and (4b). This insensitivity of $k(x)$ to nonuniformities in $A(x)$ or $\varepsilon(x)$ at the small amplitude $A_{\rm ref}$ suggests that $k_{\rm ref}(x)$ is indeed an accurate and robust reference measurement. Thus, when we actually do observe distortions in $k(x)$, it will be sensible to conclude that these are due to real dynamical effects and not just to measurement error. Indeed, we will see below that $k(x)$ becomes increasingly and systematically distorted as A_s is increased, and it will turn out that this is due to an increasing sensitivity of $k(x)$ to distortion in $A_{\rm ref}(x)$. We will therefore be led to invent a feedback algorithm that consists of modifying $A_{\rm ref}(x)$ so as to render $k(x)$ uniform. We will find that this modification causes $A_{\rm ref}(x)$ to come into agreement with the

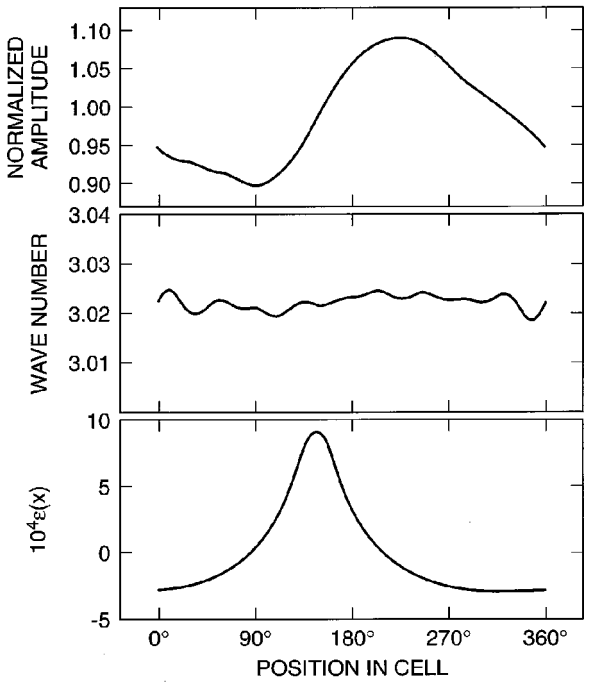

FIG. 3. Response of a TW state at $A_s = A_{\mathrm{ref}} = 0.0024$ to a strongly nonuniform Rayleigh-number profile (shown in the bottom frame). The amplitude profile, shown in the top frame, exhibits a peak in its spatial derivative that coincides with but is slightly wider than the peak in the Rayleigh-number profile. The wave-number profile (middle frame) is unaffected by the nonuniform Rayleigh number. Because this run was conducted in a cell with a slightly different geometry than that used in the rest of the experiments, the mean wave number here is slightly different from that shown elsewhere in this paper.

amplitude profile shown in the top of Fig. 1, suggesting that the original distortion in $A_{\mathrm{ref}}(x)$ measured at $A_s = A_{\mathrm{ref}}$ is just an experimental artifact due to integrated noise.

RESULTS OF EXPERIMENTS ON SPATIAL-FEEDBACK CONTROL

The quantitative data reported in the remainder of this paper were obtained by using global and spatial feedback to maintain constant and uniform amplitude and wave-number profiles over a wide range of TW amplitudes. The procedure was to change the set amplitude A_s, adjust the form of the feedback if necessary, wait for stability, and record TW data in a steady state. This was done at many different values of A_s, with periodic recalibrations at $A_s = A_{\mathrm{ref}}$. The main issues discussed in this section are the nature of the mechanisms that destabilize uniform TW's at high amplitudes and the development of appropriate feedback algorithms to control them.

To put these experiments in perspective, we begin this section with a brief description of the evolution of this system in the absence of control. This is shown in Fig. 4. Beginning with a small-amplitude, uniform TW state at $R = R_{\mathrm{ref}}$, we turn off the global feedback and increase ε slightly above zero. This leads to growth in A_m and then to the formation of a spatially localized burst of TW's. This main burst, which appears in red and yellow in Fig. 4, abruptly collapses and is followed by a weaker secondary burst (in blue-green). As described in detail in Ref. [17], this series of events, which is triggered by the instability discussed in relation to Eqs. (4a) and (4b) above, repeats several times before evolving into steady-state dispersive chaos.

Under global feedback, dispersive-chaos-like behavior is also seen, but the route to this behavior as A_s is increased follows a different scenario than that shown in Fig. 4. Uniform TW states are stable under global feedback up to $A_s = A_1 \sim 0.0029$. Above this threshold, the uniform TW state loses stability to growing, propagating amplitude modulations. Figure 5 shows the nature of this instability. In the first part of this run, made at $A_s = 0.0030$, the initially uniform amplitude profile develops diagonal stripes of increasing contrast, characteristic of the growth of the lowest spatial Fourier mode. When A_s is increased to 0.0035 (at time $t = 15$ h in the run in Fig. 5), the modulation growth rate increases. In the last ~ 15 h of this run, when the modulations have grown to high amplitude, they become spatially and temporally nonuniform. The growth of the modulation amplitude can be more easily appreciated in Fig. 6, which shows the standard deviation of the amplitude profile σ_A, normalized to the spatially averaged amplitude A_m, as a function of time during the run of Fig. 5. This measure of the nonuniformity of the amplitude profile grows exponentially for the first 15 h of this run and then shows an erratic saturation. The subsequent evolution of the system remains erratic and exhibits many of the hallmarks of dispersive chaos without global feedback.

Figure 7 shows the dependence on A_s of the growth rate γ_1 and the frequency ω_1 of the lowest-Fourier-mode amplitude modulations produced by this instability. The zero crossing of γ_1 defines the instability threshold $A_1 = 0.002\,87(4)$. The modulation frequency $\omega_1 = 0.0497(4)$ is independent of A_s. For comparison, the phase velocity of the underlying TW's corresponds to a frequency of 0.072.

Figure 8 shows the structure of the modulations produced by this instability, measured during a phase of nearly vanishing growth rate at $A_s = 0.0293(4) \approx A_1$. To reduce noise, we acquired a long data set, computed the wave-number and amplitude profiles at each time step, shifted them to a comoving frame of reference, and averaged in time. The amplitude modulations shown in Fig. 4 are accompanied by modulations in the wave number. Both profiles exhibit a nearly sinusoidal shape, with the wave-number profile lagging $125° \pm 5°$ behind (i.e., to the left of) the amplitude profile.

In order to proceed to high TW amplitudes, these modulations must be damped by imposing spatial feedback. The general principle that amplitudes grow exponentially with Rayleigh number near onset led us to choose a feedback component proportional to the logarithm of the amplitude profile. Specifically, we apply a total stress parameter $\varepsilon(x,t) = \varepsilon_g(t) + \Delta\varepsilon_1(x,t)$, where $\varepsilon_g(t)$ is the stress parameter produced by the global feedback component in Eq. (2), and

$$\Delta\varepsilon_1(x,t) = -\chi_1 \ln[A(x + \delta x_1, t)/A_s]. \tag{5}$$

Here, $\chi_1 > 0$ is a gain parameter, and $\delta x_1 \propto \omega_1$ is a spatial shift set to match the propagation of the amplitude modula-

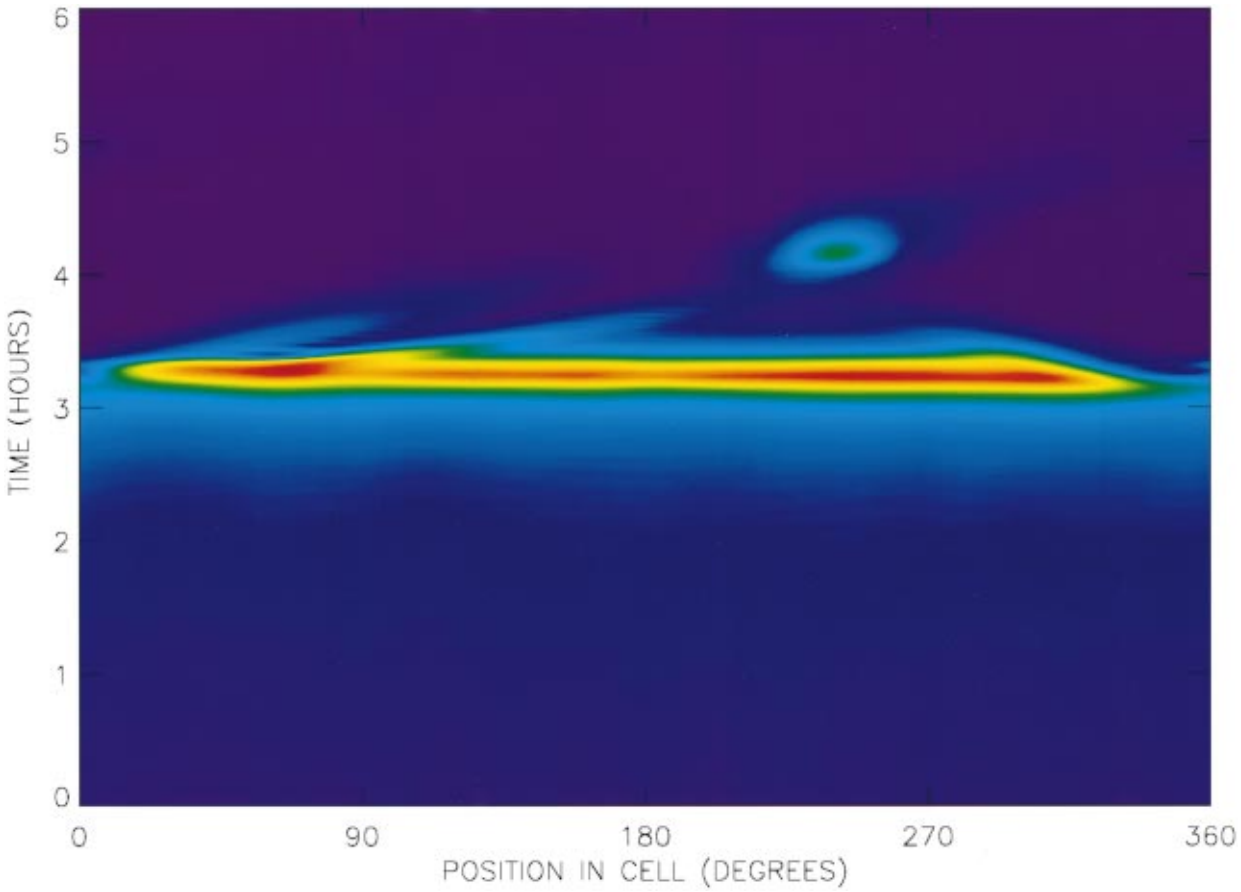

FIG. 4. (Color) False-color, space-time representation of the TW amplitude in an initially spatially uniform state of small-amplitude, right-going TW's, illustrating the growth of a burst of TW's in the absence of control. The color sequence purple–dark blue–light blue–green–yellow–red encodes increasing TW amplitude. The initial TW state was prepared under global control as described in the text. Three hours before the start of this data set, control was turned off, and the Rayleigh number was increased by a fraction $\varepsilon = 0.000\,38(5)$. This caused the TW's to grow up and form a spatially localized burst, which then collapsed. This data set is the same one that is represented by Figs. 3–7 in Ref. [17].

tion during the time delay required to calculate and apply the spatial feedback. Turning on this feedback component rapidly eliminates amplitude modulations. This is illustrated dramatically in the false-color image in Fig. 9: turning on the gain χ_1 causes an almost instantaneous flattening of the initially modulated amplitude profile. This effect is also recorded in Fig. 10, in which the fractional spatial standard deviations of the amplitude and wave-number profiles are plotted as functions of time for this run. The sharp decrease in σ_A/A_m is again clear in the top frame of the figure. The bottom frame shows that the wave-number profile requires about 8 h to become completely uniform again.

Over the range of amplitudes for which the feedback of Eq. (5) is effective, it keeps the system entirely uniform. Typically, we measure $\sigma_A/A_m \sim 0.02$ and $\sigma_k/k_m \sim 0.002$, and the applied stress-parameter profile exhibits a nonuniformity $\sigma_\varepsilon \lesssim 2-3\times 10^{-4}$. The effectiveness of this amplitude feedback is not sensitively dependent on the value of the gain parameter χ_1—changes by a factor of 2 do not degrade control once it is established. As A_s is increased, we find that χ_1 must be increased and δx_1 must be decreased in order to retain stabilization. For our update time step $\Delta t = 200-220$ sec, the values of χ_1 required for stability range from 0.005 to 0.030.

Amplitude feedback alone can maintain stability only up to a certain value of A_s. Above $A_2 = 0.010\,80(2)$, we were not able to stabilize the system only by increasing χ_1. Above this second threshold, we observe that the system loses stability to growing, propagating wave-number modulations. Their growth rate γ_2 and frequency ω_2 are shown as functions of A_s in Fig. 11. Interestingly, the modulation frequency ω_2 depends strongly on A_s, in contrast to the amplitude-independent modulation frequency ω_1 shown in Fig. 7. Figure 12 shows the structure of the modulated state produced by this second instability, recorded with $A_s = A_2$. The sinusoidal wave-number modulation is preceded in phase by a weakly nonuniform, nonsinusoidal amplitude profile. The spatial feedback of Eq. (5) causes a corresponding, inverted profile of the stress parameter $\varepsilon(x)$.

The propagating wave-number modulation seen in Fig. 12 can be thought of as a modulation in TW velocity. In uniform states of nonlinear TW's, it is well known that, as the Rayleigh number is increased, the TW amplitude increases and the TW velocity decreases [14]. This consideration led us to try to damp these modulations by adding a second spatial feedback component proportional to the gradient of the wave-number profile. That is, we applied a total stress parameter $\varepsilon(x,t) = \varepsilon_g(t) + \Delta\varepsilon_1(x,t) + \Delta\varepsilon_2(x,t)$, where

$$\Delta\varepsilon_2(x,t) = \chi_2 \partial_x k(x+\delta x_2, t). \tag{6}$$

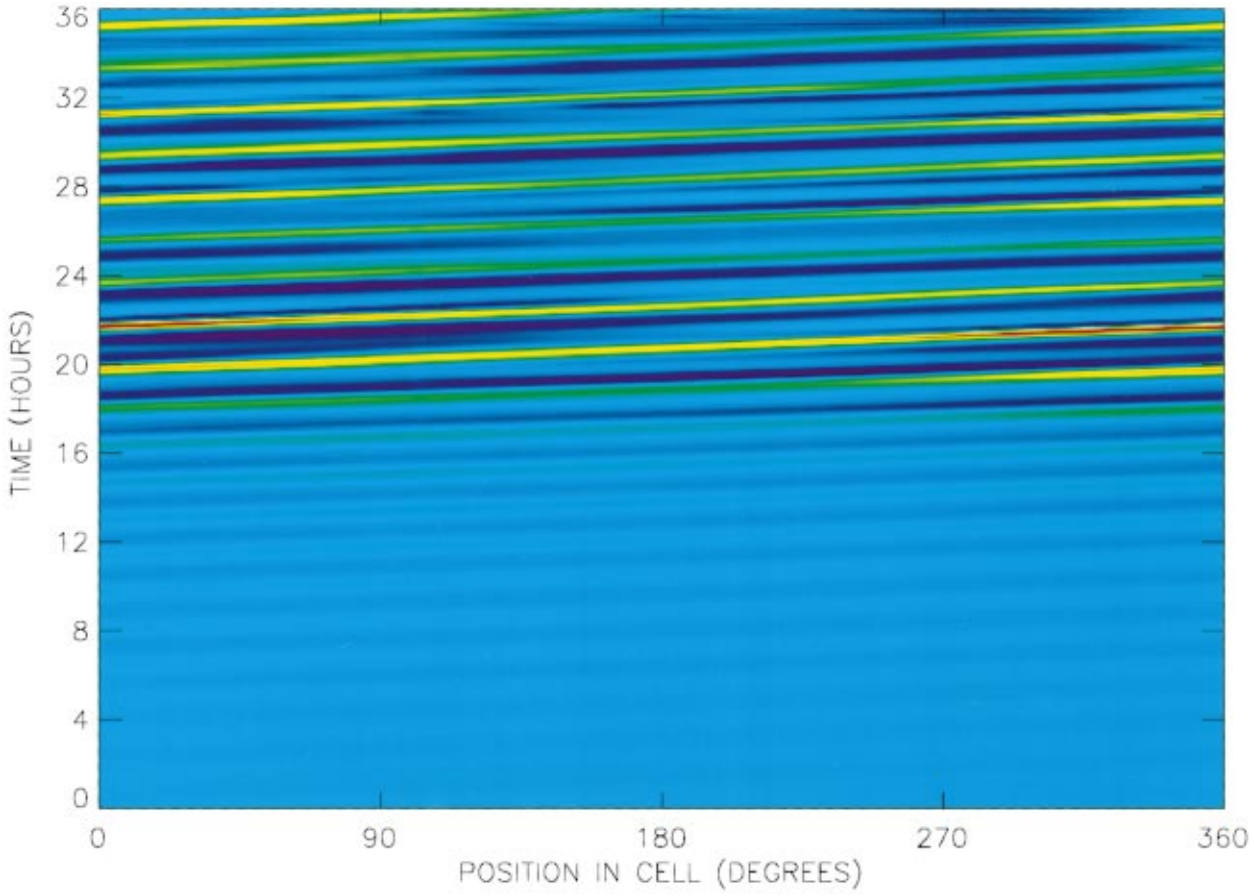

FIG. 5. (Color) False-color, space-time representation of the TW amplitude in an initially spatially uniform state of right-going TW's illustrating the growth of propagating amplitude modulations under global feedback. Initially, the set point A_s was set to 0.0030, just above the instability threshold A_1, and diagonal stripes of increasing modulation depth reveal the growth of the instability. At time $t=15$ h, A_s was further increased to 0.0035, accelerating the growth of the modulations and leading to spatial and temporal variations in their strength.

As before, χ_2 is a positive gain parameter, and the spatial shift $\delta x_2 \propto \omega_2$ compensates for propagation delay. This feedback algorithm does indeed cause the wave-number modulations due to the second instability to decay, albeit slowly, allowing the set point A_s to be stably increased well beyond the threshold A_2. As with the amplitude feedback used to suppress the first instability, stabilization is insensitive to the exact value of χ_2, but higher amplitudes require gains up to $\chi_2=1.2$.

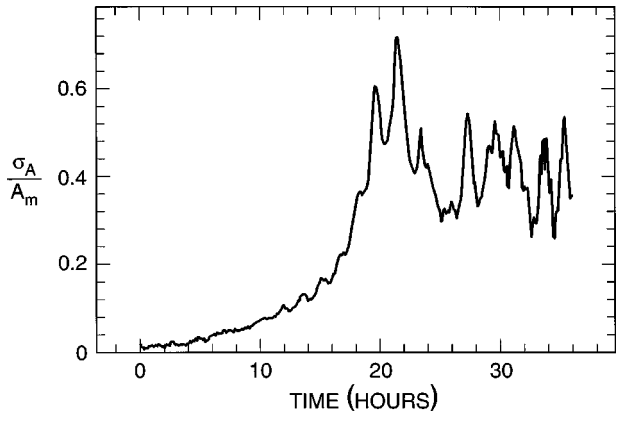

FIG. 6. The fractional amplitude nonuniformity σ_A/A_m is plotted as a function of time during the run of Fig. 5. An initial phase of exponential growth (up to $t\sim 15$ h) is followed by erratic behavior of the highly distorted amplitude profile.

Raising the set point above ~ 0.013 causes a new series of problems. With increasing A_s, the wave-number profile develops a static distortion of increasing magnitude, despite the suppression of propagating wave-number modulations by the feedback of Eq. (6). At the same time, the stress-parameter field $\varepsilon(x)$ required to keep the amplitude profile flat becomes increasingly nonuniform. Ultimately, when $k(x)$ becomes sufficiently distorted, the coupling between wave-number variations and the amplitude growth rate described above in relation to Eqs. (4a) and (4b) causes the system to become dispersively unstable and impossible to control.

It was noted above that the reference profile $A_{\mathrm{ref}}(x)$ measured at $A_s=0.0024$ appears distorted relative to the amplitude profile shown for nonlinear TW's at $\psi=-0.124$ in Fig. 1. If this distortion is real, then, in light of the source term $c_2\partial_x A^2$ in the wave-number evolution equation, Eq. (4a), forcing the TW amplitude profile to match a nonuniform reference profile may be the cause of the wave-number distortions seen at high A_s. This intuition led us to attempt to correct the amplitude distortion by modifying $A_{\mathrm{ref}}(x)$ at every time step, using a correction of the form $A_{\mathrm{ref}}(x) \rightarrow A_{\mathrm{ref}}(x)\times f(x)$, where $f(x)$ depends on the wave-number nonuniformity $\Delta k(x)\equiv k(x)-k_m$ in some way that obeys the condition $f(x)\rightarrow 1$ as $\Delta k(x)\rightarrow 0$. Clearly, since this recipe

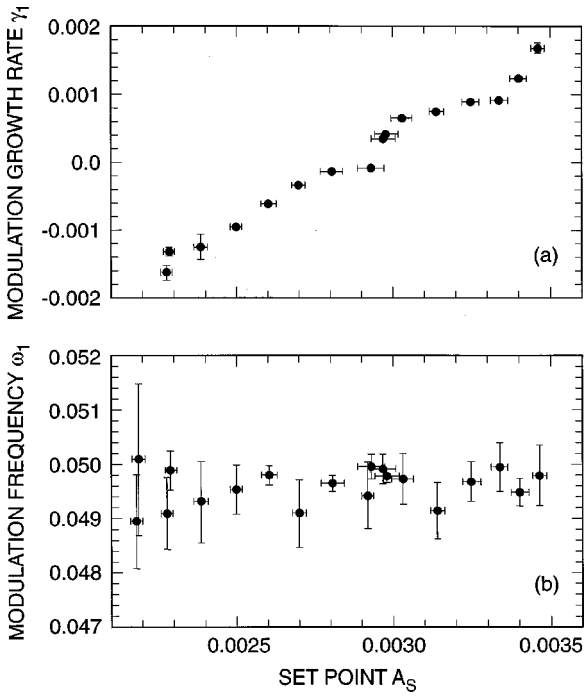

FIG. 7. The dimensionless growth rate (a) and frequency (b) of modulations of the amplitude profile with no spatial feedback are plotted as functions of the set point A_s. Above $A_s = A_1 = 0.002\,87(4)$, TW's controlled with global feedback alone are unstable and require spatial feedback.

calls for repeated multiplication of $A_{\rm ref}(x)$ by $f(x)$, this procedure must either go unstable or converge to a uniform wave-number profile, for which $f(x)=1$. If the procedure converges and the final stress-parameter profile remains uniform, then it will be very interesting to examine the final amplitude-reference profile $A_{\rm ref}(x)$.

We successfully applied this reference-profile modification scheme by implementing an algorithm inspired by Eq. (4a). The content of this equation can be paraphrased as $\partial_t \Delta k \sim \partial_x A^2$. Roughly speaking, in order to obtain a reference-amplitude profile from a measurement of $\Delta k(x)$, this suggests that we should integrate $\Delta k(x)$ in space and take the square root. On this basis, we tried a reference-amplitude correction function of the form

$$f(x) = \left[1 + \chi_f \int_0^x \Delta k(x')\,dx' \right]^{1/2}. \tag{7}$$

Despite the vagueness of the derivation of Eq. (7), we have found that, for a range of positive values of χ_f, this correction algorithm actually restores the system to a stable, uniform state. Figures 13 and 14 show the results for a run at $A_s = 0.010$. Initially, χ_f was set to 0, forcing $f(x)=1$, and $k(x)$ and $\varepsilon(x)$ were rather distorted: Fig. 13 shows that $\sigma_k/k_m \sim 0.006$ and $\sigma_\varepsilon \sim 4\times10^{-4}$ at the beginning of this run. The slight dip in σ_k/k_m at time 15 h is due to a small, accidental decrease in A_s. At time $t = 18$ h, χ_f was increased from 0 to 0.006, and this caused $k(x)$ to grow completely uniform over the next 10 h, with little change in the uniformity of $\varepsilon(x)$ or $A(x)$ [we remind the reader that amplitude uniformity refers to the flatness of the measured amplitude profile as normalized by $A_{\rm ref}(x)$, which is changing slowly due to the iterated correction of Eq. (7)]. So our first observation is that this amplitude-reference correction procedure does indeed cause the wave-number profile to grow more uniform.

A more telling indication of the correctness of this procedure is seen in the actual amplitude and wave-number profiles imposed on the system by this procedure. Figure 14 shows these profiles, *corrected using the reference profiles in Fig. 1*. The dashed curves show the profiles measured at the beginning of the period in Fig. 13, as enforced by spatial feedback whose effect is to bring the amplitude profile into agreement with the reference profile acquired at $A_s = A_{\rm ref}$. The nonuniformity of $A(x)$ shows the distortion of this reference profile with respect to that in the top of Fig. 1. The dashed wave-number profile in Fig. 14 shows the static distortion caused by imposing the incorrect amplitude profile. The full curves in Fig. 14 show the profiles measured at the end of the period in Fig. 13. The application of Eq. (7) has made both $k(x)$ and $A(x)$ come into agreement with the reference profiles shown in Fig. 1. Our conclusion is that the amplitude reference profile in Fig. 1, and not the profile measured at $A_s = A_{\rm ref}$, is the correct measure of amplitude uniformity in this system, and that the distortion in $k(x)$ is indeed caused by the error in the reference amplitude profile measured at $A_{\rm ref}$.

This reference-correction procedure has allowed us to create uniform TW's with much higher amplitudes—up to $A_m = 0.0255$—with little increase in σ_ε. However, this observation is no guarantee that the formula in Eq. (7) is exactly correct; it only shows that this procedure makes an improvement to $A_{\rm ref}(x)$ at each time step and has an effective gain that is small enough for stability.

The observation that the wave-number profile is distorted by the imposition of a distorted amplitude reference profile led us to perform a series of experiments in which we set $f(x)=1$ in Eq. (7) and measured the changes produced in $k(x)$ by abruptly changing the amplitude reference profile. We accomplished this by multiplying $A_{\rm ref}(x)$ by a time-independent, nonuniform distortion $\Delta a(x)$ which is only

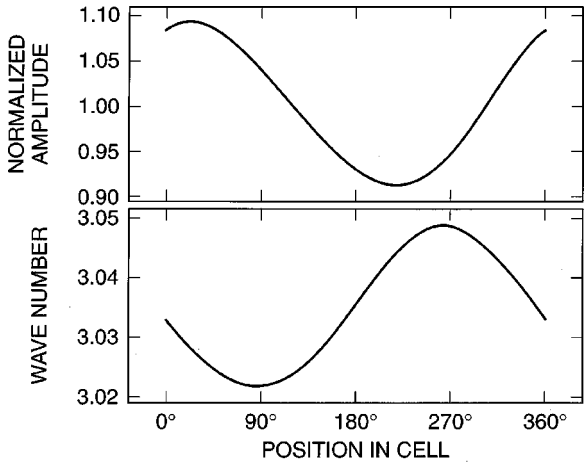

FIG. 8. Comoving time averages of the amplitude and wave-number profiles of a modulated TW state at $A_s = 0.0293(4)$. This stationary modulated state was created by first increasing A_s above A_1 to cause modulations to grow up and then decreasing A_s to $\sim A_1$ to obtain a nearly zero growth rate.

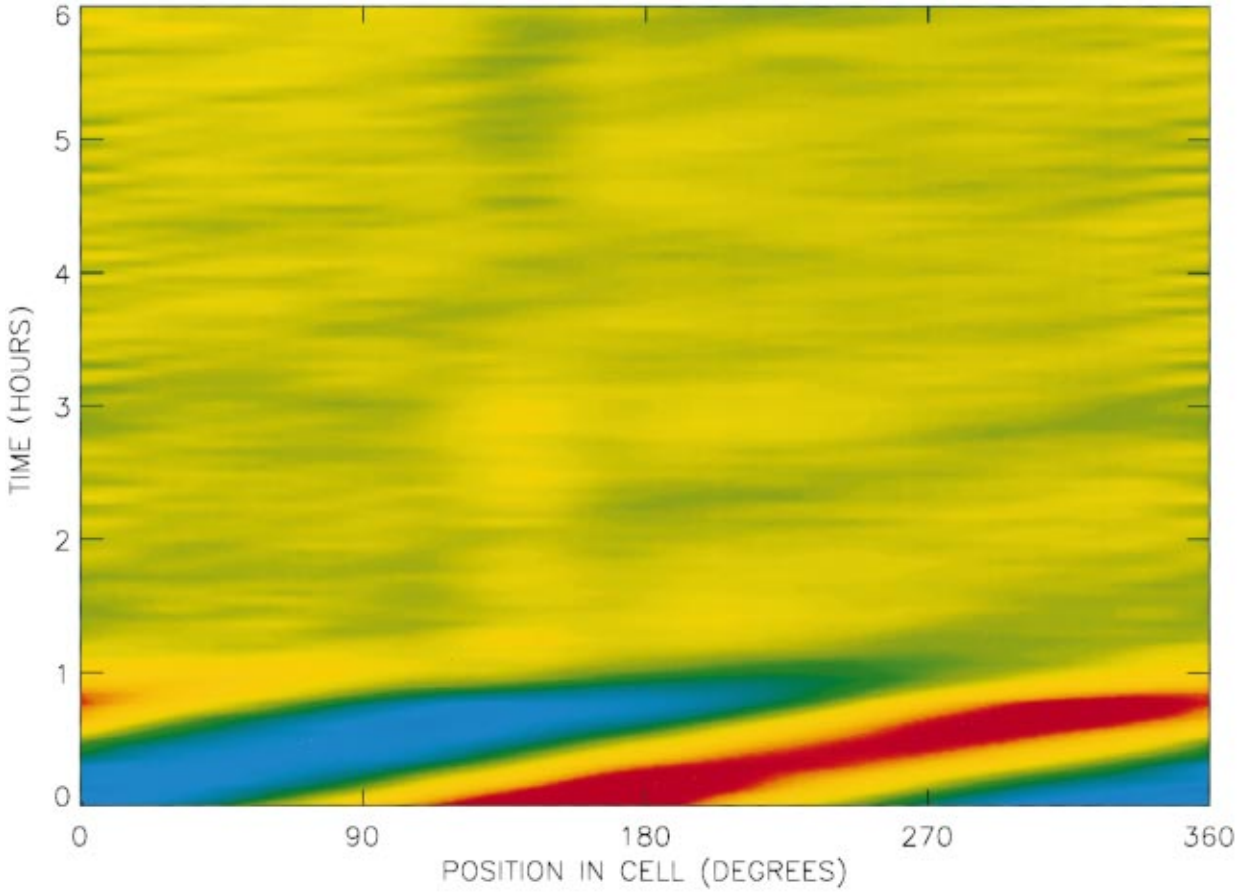

FIG. 9. (Color) False-color, space-time representation of the TW's in a state in which an initial amplitude modulation is controlled by spatial feedback according to Eq. (5). An abrupt decrease in the modulation amplitude is observed immediately after increasing the value of χ_1 from 0 to 0.005 at $t=0.7$ h.

slightly different from unity. Our results can be summarized by the statement that the imposed distortion $\Delta a(x)$ causes a wave-number distortion $\Delta k(x) \approx \alpha[\Delta a(x+\delta x)-1]$, with parameters α and δx that depend on A_s. The sensitivity of

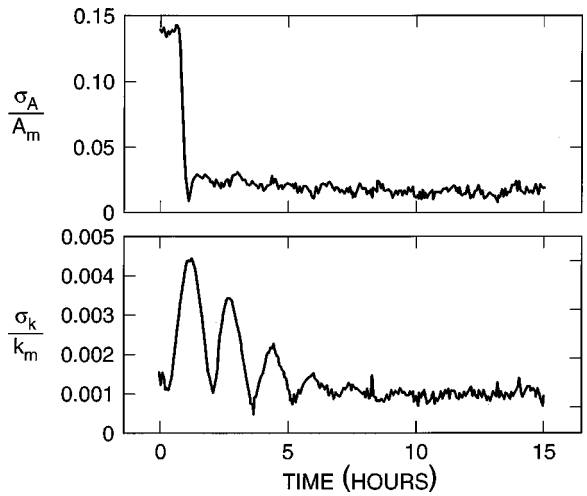

FIG. 10. The fractional standard deviations of the amplitude (top frame) and wave number (bottom) are plotted as functions of time for the run of Fig. 9. Turning on the feedback in Eq. (5) at time $t=0.7$ h causes an abrupt decrease in σ_A/A_m and a much slower decrease in σ_k/k_m.

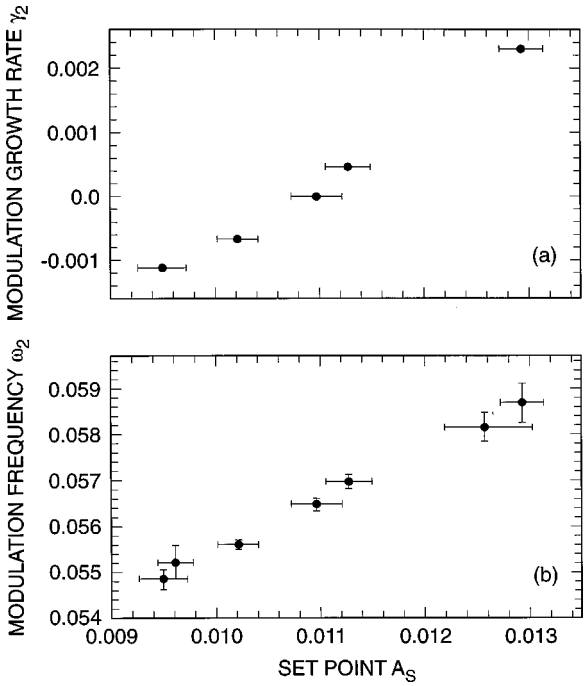

FIG. 11. The dimensionless growth rate (a) and frequency (b) of wave-number modulations observed for the closed-loop system with spatial feedback $\Delta\varepsilon_1(x)$ are plotted as functions of A_s. Above $A_s=A_2=0.010\,80(2)$, the TW's suffer a second instability and require an additional spatial feedback component.

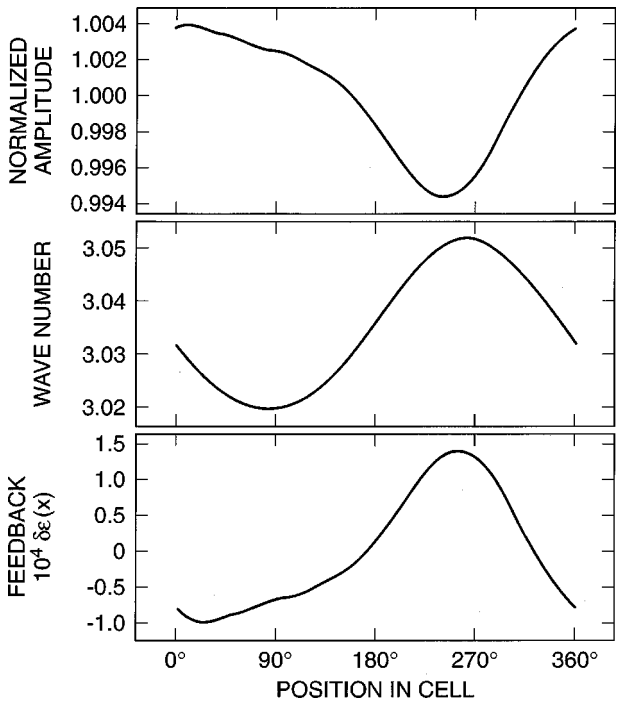

FIG. 12. Comoving time averages of the modulated amplitude, wave-number, and stress-parameter profiles of a steadily modulated TW state produced by the second instability. In contrast to the state of Fig. 8, the weak amplitude feedback shown in the bottom frame (with $\chi_1 = 0.025$) keeps the amplitude profile nearly uniform in space.

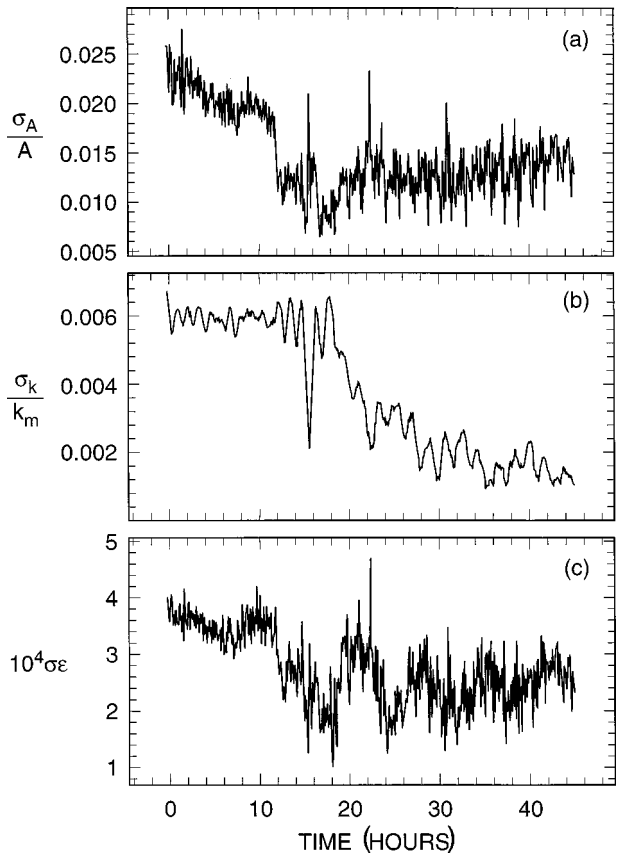

FIG. 13. Measures of the uniformity of the TW state are plotted as functions of time during a run in which the amplitude reference profile was modified at every time step according to Eq. (7). (a) Fractional spatial standard deviation of the amplitude profile. (b) Fractional spatial standard deviation of the wave-number profile. (c) Spatial standard deviation of the stress-parameter profile. Initially, χ_f was set to 0, and A_s was set to 0.010. A brief decrease in A_s between times 14.6 and 17.3 h caused the spatially averaged amplitude A_m to drop to 0.0075; this is seen in the dip in σ_k/k_m at time $t = 15.5$ h. Then, at time 18.0 h, χ_f was increased to 0.006, causing a clear decrease in the nonuniformity of the wave-number profile.

the wave-number profile to the amplitude reference profile, measured by the coefficient α, is quite strong and appears to increase with increasing A_s. This observation explains why it becomes increasingly difficult to maintain stability as A_s is increased without feedback correction of distortions in $A_{\mathrm{ref}}(x)$.

The final result of the spatial feedback described by Eqs. (5)–(7) is that a TW state with uniform amplitude and wave number can be maintained in a steady state for a wide range of TW amplitudes. The spatial variation in the Rayleigh-number profile required for stability is only $2-4\times10^{-4}$ for all the data discussed in this paper. Thus we are indeed stabilizing uniform TW states with spatial feedback of infinitesimal magnitude. An important question is whether the stability of the TW state is lost when the spatial feedback is turned off. We have not studied this issue extensively, but we have verified that the uniform state does go unstable when the control is turned off.

The final results of these experiments, shown in Fig. 15, are measurements of $\varepsilon(A_s)$ and $\Delta\omega(A_s)$ for unidirectional TW states controlled with spatial feedback. As shown in Fig. 15(a), the closed feedback loop has allowed us to trace the subcritical open-loop bifurcation diagram up to amplitudes much higher than the thresholds $A_{1,2}$ of the two secondary instabilities, which are indicated by horizontal lines. Figure 15(b) shows the amplitude dependence of the oscillation frequency. To see if these measurements are consistent with the predictions of the quintic CGLE presented in Eqs. (3a) and 3(b), we fit both data sets to a function of the form $f(A_s) = a + bA_s^2 + cA_s^4$. The best-fit functions, shown as the smooth curves in Figs. 15(a) and (b), describe the data accurately and yield the following values of the cubic and quintic coefficients in the CGLE of Eq. (1):

$$g = 13.2 \pm 0.5, \quad \tau_0^{-1} c_2 g = -754 \pm 36, \tag{8a}$$

$$h = (-7.1 \pm 1.1)\times 10^3, \quad \tau_0^{-1} c_4 h = (2.1 \pm 1.1)\times 10^5. \tag{8b}$$

The coefficients of the cubic terms in the CGLE can be compared with the less-precise values presented in Refs. [17] and [19]. In Ref. [17], we measured $\tau_0^{-1} = 9.81 \pm 0.19$ in a cell of radial width $\Gamma_r = 1.677$. With this, the measurements in Eq. (8a) yield a nonlinear frequency-renormalization coefficient $c_2 = -5.82 \pm 0.37$. This value is smaller than but still consistent with the value -7.5 ± 3.2 presented in Ref. [17]. In the wider cell used in the present work, τ_0^{-1} may be closer to the theoretical value of 9.161 ± 0.008 [17], which would imply $c_2 = -6.24 \pm 0.38$. Both of these two new estimates for c_2 lie somewhat below the range 7–12 measured in Ref. [19], but those measurements were made using a different procedure and geometry and thus may not be directly comparable with

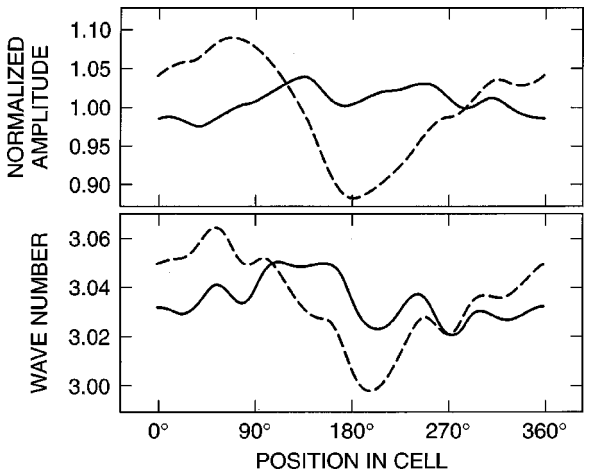

FIG. 14. Amplitude (top) and wave-number (bottom) profiles for two periods during the run of Fig. 13, corrected using the reference profiles in Fig. 1 instead of those measured at $A_s = A_{\mathrm{ref}}$. Dashed curves: nonuniform initial profiles, averaged over the period $t = 6.4$ to 12.3 hours in Fig. 13. Full curves: final profiles, averaged over the period 35.1–43.9 h in Fig. 13. Application of the correction in Eq. (7) has made $k(x)$ more uniform and has brought $A(x)$ and $A_{\mathrm{ref}}(x)$ into much better agreement with the amplitude reference in Fig. 1.

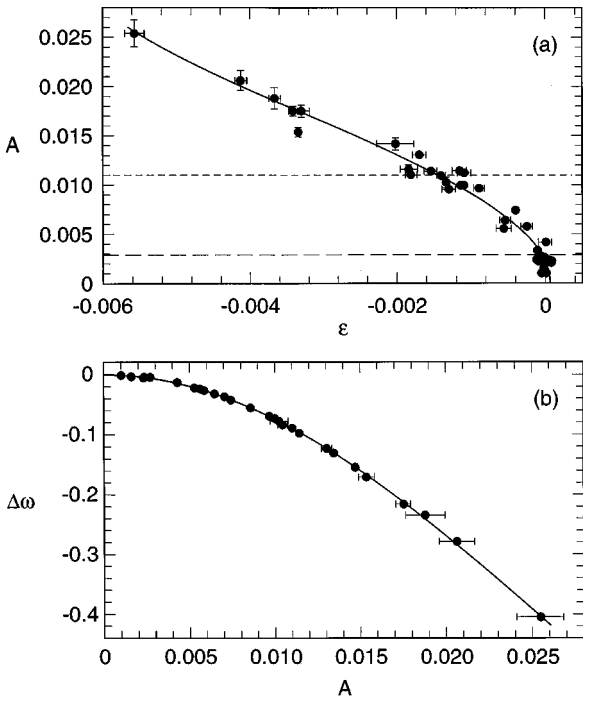

FIG. 15. (a) The stress parameter $\varepsilon(A_s)$ in controlled, uniform TW states is plotted against the set point A_s, with the axes interchanged so as to produce a bifurcation diagram. The subscript s has been dropped to emphasize the point that this is an open-loop bifurcation diagram that has been traced in closed loop. The data have been shifted slightly to give $\varepsilon(A_s \to 0) \to 0$. The long- and short-dashed lines show the instability thresholds A_1 and A_2, respectively. The curve is a fit to the solution of the CGLE given in Eq. (3a). (b) The oscillation frequency $\Delta\omega(A_s)$ is plotted against A_s. Again, the data are shifted to give $\Delta\omega(A_s \to 0) \to 0$; the actual oscillation frequency at zero amplitude is 3.14. The curve is a fit of the form given in Eq. (3b).

our results. While the analyses presented in Refs. [17] and [19] were able to yield values for the cubic coefficients in the CGLE with reasonable precision, they were certainly unable to determine the quintic coefficients at all. *The measurement of these coefficients has relied crucially on the ability to stabilize uniform TW using spatial feedback.*

DISCUSSION

In this work, we have used global and spatial feedback of infinitesimal magnitude to stabilize uniform TW's on the unstable branch of the bifurcation diagram which describes the subcritical transition to convection. Our results demonstrate that spatially distributed feedback can be used to suppress erratic spatiotemporal behavior in an extended system. This control has allowed us to trace out the unstable branch and thus to make accurate measurements of the cubic and quintic coefficients of the complex Ginzburg-Landau equation which describes uniform, unidirectional TW's in this system. These measurements, combined with the linear coefficients presented in Ref. [17] and the recent measurement of the coefficient that governs the cubic nonlinear interaction between oppositely propagating TW's [22], constitute a complete quantitative description of weakly nonlinear TW convection in this experimental system. In order to extend this model so that it quantitatively describes dispersive chaos, two further ingredients will be required. They are (i) a measurement of the coefficients of nonlinear gradient terms in the CGLE [23] and (ii) a quantitative accounting of the interaction between TW's and the ethanol concentration field, which is known to have a profound effect on the behavior of high-amplitude convection [17,24].

We have found that the closed-loop system exhibits two interesting modulational instabilities. The first of these, characterized by propagating amplitude and wave-number modulations under global feedback alone, has been observed in numerical simulations of the CGLE [25]. Amplitude feedback suppresses the amplitude modulations produced by this instability, and this then causes wave-number modulations to decay. The second, a phase instability suffered under amplitude feedback, has not been considered previously. Suppression of this second instability is accomplished by spatial feedback proportional to the gradient of the wave number.

Our ability to maintain control of this system is affected by experimental imperfections such as noise and distortions in the shadowgraph signals and delays in the application of feedback, as well as by intrinsic properties of the dynamics such as the size of the basin of attraction of the controlled state. Our understanding of these issues is imperfect and variable. For example, we have little knowledge of the nature of the basin of attraction of the controlled state beyond our empirical understanding of how nonuniform a TW state can become before control is lost. Our experience is that the delays in our feedback are short enough that they do not affect the stability of the closed-loop system. The issue we understand the best is the effect of distortions in the computed amplitude and wave-number profiles: a distorted TW state cannot be brought stably to high amplitudes, and the distortion must be corrected if control is to be maintained. This aspect of our dynamical system has taught us what the uniform TW state actually is: it is the state whose amplitude

and wave-number profiles match those shown in Fig. 1, as opposed to that observed at the small TW amplitude A_{ref}, in which the amplitude profile is distorted by noise.

The results of these experiments have certain limitations. We were not able to continue tracing the unstable branch of the bifurcation diagram up to the saddle node and onto the postulated stable upper branch. This was due not to limitations of the techniques employed but to a catastrophic failure of the experimental apparatus. We did not make a serious study of the loss of stability following cessation of spatial feedback, due to lack of time. And we did not attempt to perform full control of dispersive chaos—that is, to force the system into a stable TW state, starting from an erratic state. This is discussed below.

The techniques developed in these experiments open up a wide range of interesting experiments. Here, we suggest three avenues of future research:

(i) Control of the Eckhaus instability. The Eckhaus instability of fully nonlinear TW's manifests itself in propagating wave-number modulations which are triggered when the Rayleigh number is brought below a wave-number-dependent threshold [14]. This behavior is quite similar to that produced by the second instability described in Figs. 11 and 12 and should be susceptible to suppression by spatial feedback of the form described by Eq. (6). Indeed, we routinely apply such feedback ''by hand'' to control this instability, so as to put the system into the $N_r=44$ state of Fig. 1 and create a reproducible reference state. By suppressing the Eckhaus instability, a measurement of the true marginal stability curve could be made.

(ii) Control of unstable pulses. The drifting pulses described in Ref. [15] give way to dispersive chaos as ψ is increased from -0.07 to -0.04 [16]. There is quite possibly a range of intermediate ψ in which TW pulses are only weakly unstable. These might be susceptible to control by spatial feedback, using as-yet-undetermined control algorithms.

(iii) Full control of dispersive chaos. At $\psi=-0.02$, the dynamics of steady-state dispersive chaos are influenced both by the interaction between bursts of oppositely propagating TW's and by the interaction between TW's and the ethanol concentration field [24]. While the fast demodulation routine we have developed for the present experiments on unidirectional TW's could easily be extended to separate the opposite TW components for individual control, it is hard to imagine how spatial feedback could be used to couple to the slow diffusion of ethanol and control its effect on the TW's. For this reason, we have avoided tackling this difficult problem by only starting our experiments in a state of small-amplitude, unidirectional TW's. However, as ψ is made less negative, the nonlinear dispersion responsible for dispersive bursting becomes stronger [19], and it is reasonable to expect that the effects of the concentration field on the TW's become weaker. Thus it appears likely that there is a regime of ''pure dispersive chaos'' at small $|\psi|$ in which concentration effects are unimportant relative to nonlinear dispersion. A very simple spatial feedback scheme could be used to suppress this pure dispersive chaos. Recall from the discussion of Eqs. (4a) and (4b) above that the wave-number deviations pumped by localized amplitude gradients reinforce those gradients in turn by reducing the local linear growth rate, which is proportional to $\varepsilon-\xi_0^2\Delta k^2$ [here, we have retained the parameter ξ_0^2, which was set to unity for convenience in the derivation of Eqs. (4a) and (4b)]. This feedback loop can be cut by applying the spatial feedback component

$$\Delta\varepsilon_3(x,t)=\chi_3\xi_0^2\Delta k^2(x,t). \tag{9}$$

We have found in numerical simulations of the CGLE that turning on spatial feedback of this form completely homogenizes an initial state of dispersive chaos [25], for a range of gains χ_3 near unity. In fact, it was our initial intention to use this control algorithm to stabilize our experimental TW's, but, in practice, we have never allowed the wave-number profile to become sufficiently nonuniform to trigger this instability mechanism. It appears likely that this form of spatial feedback would allow full control of pure dispersive chaos at small separation ratio.

ACKNOWLEDGMENTS

We would like to thank Ioannis Kevrekidis for extensive discussions, advice, and collaboration during the course of this work. G.F. gratefully acknowledges the financial support of the Deutsche Forschungsgemeinschaft.

[1] E. Ott, C. Grebogi, and J. A. Yorke, Phys. Rev. Lett. **64**, 1196 (1990).

[2] T. Shinbrot, Adv. Phys. **44**, 73 (1995).

[3] G. Hu and Z. Qu, Phys. Rev. Lett. **72**, 68 (1994); G. A. Johnson, M. Löcher, and E. R. Hunt, Phys. Rev. E **51**, R1625 (1995); R. O. Grigoriev, M. C. Cross, and H. G. Schuster, Phys. Rev. Lett. **79**, 2795 (1997); D. A. Egolf and J. E. S. Socolar, Phys. Rev. E **57**, 5271 (1998).

[4] D. Auerbach, Phys. Rev. Lett. **72**, 1184 (1994); J. H. Xiao, G. Hu, J. Z. Yang, and J. Gao, *ibid.* **81**, 5552 (1998).

[5] G. Hu and K. He, Phys. Rev. Lett. **71**, 3794 (1993); I. Aronson, H. Levine, and L. Tsimring, *ibid.* **72**, 2561 (1994).

[6] W. Lu, D. Yu, and R. G. Harrison, Phys. Rev. Lett. **76**, 3316 (1996); R. Martin, A. J. Scroggie, G.-L. Oppo, and W. J. Firth, *ibid.* **77**, 4007 (1996); D. Battogtokh and A. Mikhailov, Physica D **90**, 84 (1996); M. E. Bleich and J. E. S. Socolar, Phys. Rev. E **54**, R17 (1996); M. E. Bleich, D. Hochheiser, J. V. Moloney, and J. E. S. Socolar, *ibid.* **55**, 2119 (1997).

[7] S. Bocaletti, D. Maza, H. Mancini, R. Genezio, and F. T. Arecchi, Phys. Rev. Lett. **79**, 5246 (1997).

[8] F. Qin, E. E. Wolf, and H.-C. Chang, Phys. Rev. Lett. **72**, 1459 (1994); see also C. Lourenço, M. Hougardy, and A. Babloyantz, Phys. Rev. E **52**, 1528 (1995); I. Triandaf and I. B. Schwartz, *ibid.* **56**, 204 (1997); and Th. Pierre, G. Bonhomme, and A. Atipo, Phys. Rev. Lett. **76**, 2290 (1996).

[9] L. Howle, Int. J. Heat Mass Transf. **40**, 817 (1997); Phys. Fluids **9**, 1861 (1997); *ibid.* **9**, 3111 (1997).

[10] J. Tang and H. H. Bau, Phys. Rev. Lett. **70**, 1795 (1993); J. Fluid Mech. **363**, 153 (1998).

[11] P. Kolodner, A. Passner, C. M. Surko, and R. W. Walden, Phys. Rev. Lett. **56**, 2621 (1986).

[12] P. Kolodner and H. Williams, in *Proceedings of the NATO*

Advanced Research Workshop on Nonlinear Evolution of Spatio-temporal Structures in Dissipative Continuous Systems, Vol. 225 of *NATO Advanced Study Institute, Series B2*, edited by F. H. Busse and L. Kramer (Plenum, New York, 1990), p. 73.

[13] P. Kolodner, H. Williams, and C. Moe, J. Chem. Phys. **88**, 6512 (1988).

[14] P. Kolodner, Phys. Rev. A **46**, 6431 (1992); **46**, 6452 (1992).

[15] P. Kolodner, Phys. Rev. A **44**, 6448 (1991); **44**, 6466 (1991).

[16] P. Kolodner, J. A. Glazier, and H. Williams, Phys. Rev. Lett. **65**, 1579 (1990); J. A. Glazier, P. Kolodner, and H. Williams, J. Stat. Phys. **64**, 945 (1991).

[17] P. Kolodner, S. Slimani, N. Aubry, and R. Lima, Physica D **85**, 165 (1995).

[18] P. Kolodner, G. Flätgen, and I. G. Kevrekidis, Phys. Rev. Lett. **83**, 730 (1999).

[19] E. Kaplan, E. Kuznetsov, and V. Steinberg, Phys. Rev. E **50**, 3712 (1994).

[20] E. Kaplan, E. Kuznetsov, and V. Steinberg, Europhys. Lett. **28**, 237 (1994).

[21] Xicor Corp., Milpitas, CA; http://www.xicor.com.

[22] H. U. Voss, P. Kolodner, M. Abel, and J. Kurths, Phys. Rev. Lett. **83**, 3422 (1999).

[23] R. J. Deissler and H. R. Brand, Phys. Lett. A **146**, 252 (1988); Phys. Rev. Lett. **81**, 3856 (1998).

[24] H. Riecke, Phys. Rev. Lett. **68**, 301 (1992); Physica D **61**, 253 (1992).

[25] G. Flätgen, I. G. Kevrekidis, and P. Kolodner (unpublished).